Surface & Coatings Technology 514 (2025) 132547

Contents lists available at ScienceDirect

Surface & Coatings Technology

journal homepage: www.elsevier.com/locate/surfcoat

Modeling and in-flight diagnostics of the IN718 cold spray process using different nozzle geometries☆

J. Schmitt [a,*], G. Mauer [a,b], R. Mücke [a], J. Fiebig [a], O. Guillon [a,c], R. Vaßen [a,d]

[a] Forschungszentrum Jülich GmbH, Institute of Energy Materials and Devices, IMD-2: Materials Synthesis and Processing, Jülich, Germany
[b] Technische Universität Dortmund, Department of Mechanical Engineering, Dortmund, Germany
[c] Jülich Aachen Research Alliance: JARA-Energy, 52425 Jülich, Germany
[d] Institut für Werkstoffe, Ruhr-Universität Bochum, Bochum, Germany

ARTICLE INFO

Keywords:
Cold Spray - Inconel 718
Modeling
Spray spot
Particle diagnostics

ABSTRACT

The cold gas spray process has emerged as a promising thermal spray technology since its introduction in the 1980s, offering lower operating temperatures and reduced oxidation effects compared to conventional thermal spray methods. This paper presents a comprehensive investigation of cold gas spray dynamics using Inconel 718 as a coating material. It focuses on particle diagnostics and numerical simulations associated with three commercially available nozzle geometries for the cold gas spray system used. Key findings include particle velocity measurements using two diagnostic instruments – a cold spray meter and a HiWatch system – compared with simulation models to analyze the relationship between particle trajectory and gas flow characteristics. Emphasis is placed on predicting the spray spot sizes, considering factors such as the type of powder injection (axial aligned or perpendicular orientated) and particle-flow interactions as determined by the divergent nozzle section. The spray profiles from both simulation and experiment showed a good agreement for the three nozzles, given the applied harsh spraying conditions of 4 MPa and 950 °C of the gas. The respective shock diamond structure did not significantly affect the particle dispersion, while a radial particle injection increased the overall particle velocity and temperature. Consistent particle velocities were obtained from both modeling and diagnostic tools for each of the three nozzles. In-situ curvature measurements revealed a general compressive residual stress state, which increases with larger spot size but not necessarily with the length of the divergent nozzle section as shown by findings from the CFD model.

1. Introduction

The cold gas spray process (CGS) is a relatively new thermal spray technology introduced in the 1980s in Novosibirsk [1]. Compared to conventional thermal spray methods, CGS operates at significantly lower temperatures, making it a promising alternative for repairing materials sensitive to oxidation and phase transformations [2–6]. In this process, a powder feedstock is injected into a high-velocity gas stream, typically composed of nitrogen or helium, which is preheated in an extended pre-chamber. The particles are then accelerated through a de Laval nozzle, achieving velocities between 300 and 1200 m/s while remaining below their melting point. Upon impact with the substrate at a controlled standoff distance, the particles undergo plastic deformation and adhere via adiabatic shear instability (ASI), a widely accepted bonding mechanism in CGS [7,8]. For successful deposition, the particles must exceed a material-specific critical velocity, which is influenced by both velocity and temperature. While an insufficient velocity prevents bonding, excessive velocity results in erosion rather than adhesion. The effect of temperature and velocity on the deposition efficiency (DE) is described by the 'Window of Deposition (WoD)' [9,10].

For a well-developed knowledge of process parameters and thus interaction of particle and gas flow on the background of bonding process, high-quality particle diagnostics including validating experiments are indispensable. For CGS, mainly measurements by using a DPV-system [11–13], particle image velocimetry (PIV) [14], particle tracking velocimetry (PTV) [15,16] or two laser method [17] have been carried out. The employment of a DPV 2000-type cold spray meter (CSM), equipped with a laser light source, facilitates the illumination of particles with low temperatures in CGS and the detection of thermal

☆ This article is part of a Special issue entitled: '11RIPT' published in Surface & Coatings Technology.

* Corresponding author.
E-mail address: jo.schmitt@fz-juelich.de (J. Schmitt).

https://doi.org/10.1016/j.surfcoat.2025.132547
Received 31 October 2024; Received in revised form 1 May 2025; Accepted 6 August 2025
Available online 7 August 2025

Abbreviations

ASI	Adiabatic Shear Instability
APS	Atmospheric Plasma Spray
CGS	Cold Gas Spray
CSM	Cold Spray Meter
DE	Deposition Efficiency
KSS	Kinetic Spray Solution
ICP	In-situ Coating Properties sensor
IN718	INconel 718
PIV	Particle Image Velocimetry
PTV	Particle Tracking Velocimetry
WoD	Window of Deposition

List of symbol

μ	Dynamic viscosity, [10^{-6} Pa s]
A	Cross-sectional area, [mm^2]
C_D	Drag coefficient, [−]
C_L	Lift coefficient, [−]
d	Diameter, [mm]
d_{50}	Mean diameter, [mm]
E_s	Young's modulus, substrate, [GPa]
f	External forces, [kg m s^{-2}]
F_D	Drag force, [kg m s^{-2}]
F_L	Lift force, [kg m s^{-2}]
k	Turbulent kinetic energy, [m^2 s^{-2}]
L	Length/distance, [mm]
m	Mass, [kg]
N_p	Relative amount of particles, [%]
P	force exerted by pressure differences, [kg m^{-3} s^{-2}]
R	Radius of the fitted circle, [m]
T	Temperature, [K]
t	Time, [s]
t_c	Thickness, coating, [mm]
t_{div}	Interaction time of particle and gas within the divergent nozzle section, [ms]
t_s	Thickness, substrate, [mm]
u	Velocity, gas, [m/s]
v	Velocity, particle, [m/s]
V_p	Volume of the particles, [m^3]
x_i	Cartesian coordinate in the i-direction (i = 1,2,3), [m]
κ	Curvature, [m^{-1}]
ν_s	Poisson ratio, substrate, [−]
ρ	Density, [kg m^{-3}]
σ_{St}	Residual stress, obtained from the Stoney equation, [MPa]
ω	Specific dissipation rate, [s^{-1}]

List of subscripts and superscripts

*	Nozzle throat
c	Coating
con	Convergent nozzle section
div	Divergent nozzle section
exit	Nozzle exit
g	Gas
H	HiWatch
i	Spatial coordinate variable (1,2,3)
in	Nozzle inlet
j	Einstein summation of j = 1, 2, 3
loc	Local, referred to the gas spot
M	Modeled
o	Outlet
p	Particle

emission [11,12]. While such a device is typically focused on the spot of the particle plume with the highest detection rate, volumetric measurement of the particle plume can be carried out by using high-resolution PIV-systems, such as the HiWatch device [18].

Modeling particle velocity is essential for optimizing cold spray dynamics. Various models analyze deformation, thermal history, and impact velocities in relation to bonding quality [19–22]. Other authors formulated the theory of the bonding model in cold spray in terms of material properties and process parameters [19,23]. A simplified, one-dimensional modeling approach of the gas flow within a convergent-divergent nozzle geometry has been presented by several authors [8,9,19].

Particle trajectory is primarily influenced by gas flow characteristics such as turbulence, heat transfer, and drag coefficient [24]. Numerous studies have examined initial conditions, spray distance, and impact angle on deposition [25–28]. Flow modeling highlights the role of Mach disk formation, caused by pressure differences, in altering velocity magnitude [29–31]. The findings underline the importance of a fitting nozzle geometry design for an ideal expanded gas flow regarding length and exit diameter. The geometry also affects the evolving bow shock effect, which might not only decelerate the particles but is also expected to deflect particularly small particles in the radial direction and therefore improve the dispersion of the particle plume [32]. As the gas undergoes expansion within the divergent nozzle, particles exhibit a tendency to align with the flow, with drag exerting a significant influence [11,33,34]. In addition, spherical particles are also affected by a lift force. This force is a result of the velocity difference between the two sides of the particle, where the arising pressure difference produces a rotation. The lift force has been considered as relevant for uniform flows and should also be present for geometries at varying cross sections, where the velocity profile differs in radial direction [35–37].

Not only for repair but especially for additive manufacturing applications, it is essential to control the size of the spot at sufficient deposition efficiency [38–40]. At the same time, it is necessary to be aware of the arising residual stress state since the size of the spot and, therefore, profile corresponds to the enveloped stresses, possibly causing cracking and delamination [41–44]. Spray spots of small width have been reported by Ozdemir and Widener using aluminum powder in an axially aligned powder injection by keeping the inlet size below the nozzle throat diameter [45] and Sova et al. by applying a micro nozzle at significantly decreased dimensions for aluminum and copper coatings [46,47]. The type of injection might also affect the particle trajectory regarding their initial kinetic energy and drag due to non-symmetrical flow and radial velocity [48].

The modeling and experiments used in the literature typically refer to copper or aluminum powder while keeping the initial conditions for temperature and pressure at a low level. In this paper, IN718 is used as a coating material at elevated conditions for temperature and pressure on the background of suitable repair material utilizing this material for gas turbine components. Hence, the present investigation aims to implement a computational model for suitable prediction of gas flow properties and spot sizes within the scope of these conditions. The CFD model results are first validated against the results of in-flight analysis devices, such as the CSM and HiWatch, for a specific, commercially available nozzle geometry. The modeling and experimental techniques are then employed to two other commercially available, varied nozzle geometries. The arising residual stress for each nozzle is investigated by analyzing the in-situ curvature and discussed in the scope of the nozzle geometry and the associated gas properties.

2. Material and methods

2.1. Cold spray setup

The cold spray process was performed on the Impact 5/11 system (Impact Innovations GmbH, Rattenkirchen, Germany) with a water-cooled de Laval nozzle and nitrogen (grade 5.2) as propellant gas. 950 °C and 4 MPa were chosen as inlet gas temperature and pressure for deposition and particle diagnostics, respectively. A spray angle of 90° and a 60 mm spray distance between the nozzle exit and substrate surface were selected for all the experiments. The surface speed of the spray gun (by means of the velocity for passing the substrate surface) was 500 mm/s. Powder particles are injected radially into the nozzle at a constant powder feed rate of 24 g/min. This setup has been successfully implemented in previous studies [11,41,49] and applied to all nozzle geometries (see below).

An IN718-powder (Oerlikon-Metco, Troy, MI, USA) with spherical morphology (d_{10} = 9.5 µm, d_{50} = 14 µm, d_{90} = 20 µm) was used as coating material. The powder, which has been patented by Oerlikon, contains a substantial quantity of enriched nickel-aluminum phases and is asserted to provide a dense and well-adhering coating as a consequence of this blended phase [25]. The feedstock powder was used for in-flight particle analyses and deposited on polished stainless steel substrates with dimensions of 30 mm × 30 mm × 3 mm.

A single line profile with 8 deposition passes have been deposited to ensure a sufficient coating build-up and the formation of characteristic wall angles [50]. Such spray profiles are called 'line profiles (LP)' from here on. For the ICP-samples, a spray meander with sufficient length and 1 mm vertical stand-off distance between each line has been used.

Three different types of commercially available nozzle geometries were used for the experiment and modeling. These nozzles are named Out1, Out2 and Out4 based on the official nomenclature. In general, each nozzle is a de Laval nozzle (see Fig. 1) with characteristic dimensions given in Table 1. A more detailed examination of the particle injection is provided in the context of the modeling framework.

2.2. In-flight particle diagnostic

In order to evaluate the in-flight particle properties, the CSM and HiWatch devices have been applied at the same spray distance of 60 mm as for the substrates.

The HiWatch HR2 (Oseir Ltd., Tampere, Finland) is displayed in Fig. 2a. Its measurement volume covers a size of 8 mm × 6 mm × 0.4 mm (Fig. 2b). The particles that pass through the slit are illuminated by the light source and subsequently captured by the high-resolution camera (Fig. 2c). The implementation of the shadow-imaging technique, which is based on the localized extinction of the laser light, enables the identification of the particles as bright spots depending on their size. This technique enables the measurement to be largely independent of material properties. A more detailed description of the setup is given by Koivuluoto et al. [18]. 1000 particles have been analyzed per experiment.

Table 1
Applied dimensions of Out1, Out2 and Out4 for the modeling. The expansion ratio is the ratio between cross-sectional areas of nozzle exit and throat.

	Var	Unit	Out1	Out2	Out4
Diameter, nozzle inlet	d_{in}	[mm]	13	13	13
Diameter, nozzle throat	d^*	[mm]	2.7	2.7	2.7
Diameter, nozzle exit	d_{exit}	[mm]	6.5	8.5	7.3
Diameter, atmospheric outlet	d_o	[mm]	30	30	30
Length, pre-chamber	L_{pre}	[mm]	43	43	43
Length, convergent part	L_{con}	[mm]	32	32	32
Length, divergent part	L_{div}	[mm]	130	78	180
Spray distance	L_{sub}	[mm]	60	60	60
Expansion ratio	A_{exit}/A^*	[−]	5.8	9.91	7.31

Alternatively, a cold spray meter CSM EVOLUTION (Tecnar Automation Inc. *St.* Bruno, QC, Canada) has been applied (see Fig. 2d). Here, a continuous diode laser (wavelength: 790 nm, power: 3.3 W) is used to illuminate the particle plume perpendicular to the spray direction (Fig. 2e). A dual-slit photomask is located in front of a photo-optical sensor, collecting the light scattered from individual particles at a working distance of 100 mm. Subsequently, the system generates a double-peak or twin-peak signal at the dual-slit photomask (Fig. 2f). Assuming that the measured energies correspond to a spherical particle surface, the particle velocity is calculated by the distance between the two slits and the signal time difference. A more detailed description is given by Mauer et al. [12].

2.3. Characterization methods

Every specimen is weighted before and after the deposition to evaluate the deposition efficiency of spot and line profiles. The thickness of the line profiles was measured using the P-CHR-1000 sensor of the optical profilometer Model CT350T (cyberTECHNOLOGIES GmbH, Eching-Dietersheim, Germany). For the substrate and the as-sprayed specimen from the curvature measurement, a micrometer screw has been used. The P-CHR-10000 sensor was also utilized for the post-deposition curvature measurement and size of the spot profiles.

Residual stress measurements have been carried out for the three nozzle geometries using the In-situ coating properties sensor (ICP Sensor, Reliacoat Technologies LCC, East Setauket, USA). IN718 samples have been used with the size of 228.0 mm × 25.4 mm × 3.2 mm to monitor the curvature of the specimen during deposition. Three lasers were used to monitor the displacement during the subsequent deposition cycles on both sides fixtured specimen. The temperature on the back of the substrates is obtained via two thermocouples on both supports. The Stoney Equation (Eq. (1)) has been used to convert the curvature into the corresponding residual stresses [51]:

$$\sigma_{St} = \frac{E_s' t_s^2}{6 t_c} \Delta\kappa \tag{1}$$

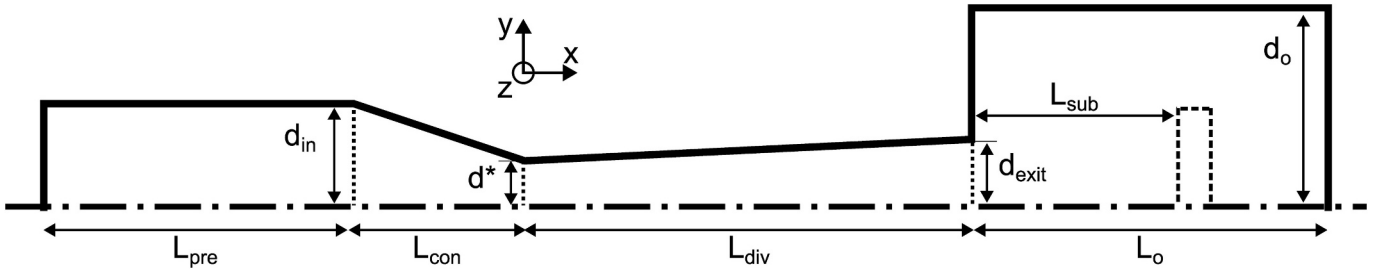

Fig. 1. Schematic sketch of the nozzle dimensions based on Table 1. The substrate boundary was employed to extract particle data from a rectangular area with dimensions of 30 × 30 mm and a thickness of 3 mm. Since the substrate was not present for all computational models it is marked in dashed lines. 'd' is referenced to the full diameter. The coordinate system is marked above the throat.

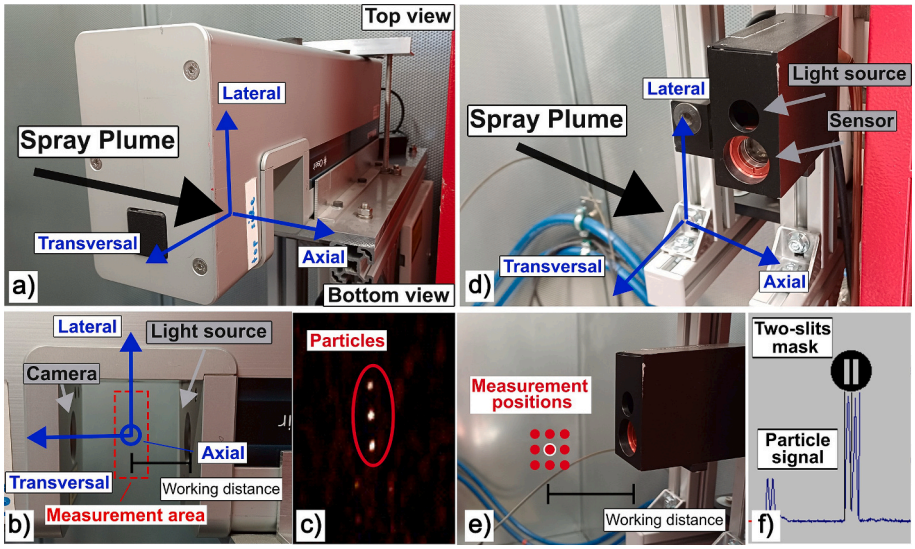

Fig. 2. The HiWatch system analyses the passing spray plume (a) within a measurement 'area' in three directions (b). Particles are shown bright by applying a light source and a camera (c). The CSM gathers the backscattered light of crossing particles (d). Only the central point (white) of the exemplary 3 × 3 scatter (red) was analyzed (e), resulting in a twin-peak signal (f).

where σ is the calculated residual stress, $\kappa = 1/R$ is the curvature over the subsequent deposition passes (R is the radius of curvature), E'_s, t_s, and t_c are the in-plane elastic modulus ($E' = E/(1-\nu)$) and thickness of substrate and coating, respectively. The arising error for thick coatings has been covered accordingly to previous studies [41]. The properties of the substrate are given in Table 2, while the coating thickness was kept constant at ~700 µm. For a more detailed description, the authors refer to previous publications using the same experimental setup [41,52].

3. Modeling framework

3.1. Geometry and boundaries

Based on the dimensions in Table 1, a computational fluid dynamics (CFD) – model in ANSYS Fluent (Ansys, Inc., Pennsylvania, USA) has been implemented. Each nozzle is sectioned in pre-chamber, convergent, and divergent parts enclosed by walls with an inflation layer for increased solution accuracy (Fig. 3a). The pre-chamber has one separated pressure-inlet each for carrier gas and process gas. No-slip condition has been applied on all nozzle walls. In each zone, an individual mesh according to the given geometry data was used. The initial conditions were applied accordingly to the experimental setup. Atmospheric conditions have been applied on the outlet surrounding the spray chamber with a substrate as required. Based on the applied geometry, the total number of elements is typically larger than 10,000,000, reaching a sufficient minimal orthogonal quality (> 0.1). The cross-sectional, simplified view of the three-dimensional model is given in Fig. 3b.

In the framework of this study, the influence of the injection design was investigated. First, particles and gas injection were spatially separated in the axial direction as shown in Fig. 3c. Apart from whether this type of injection was used, the CFD model represents a simplified approach due to the axis symmetrical setup. It should be noted that this approach may not properly describe the actual setup of the Impact 5/11, whereby the powder is transported by the carrier gas entering a partwise hollow cylinder perpendicular to the axis (see Fig. 3d). The main proportion of carrier gas enters the pre-chamber in a radial direction, even if there is an axially orientated drill hole. For this reason, this type of injection is considered 'radial' in this study. The inlet diameter of the drill hole and the axial distance to the throat have been kept in the same ratio as for the axial injection process, thus ensuring consistency in the transition area for both the process and the carrier gas. At this location, the mesh resolution was increased.

Table 2
Young's modulus and Poisson ratio and thickness of the utilized IN718 substrate material [41].

Material	E [GPa]	ν [−]	t_s [mm]
IN718 substrate	200	0.29	3.2

3.2. Equations governing gas-flow and discrete phase

Solving the gas stream motion is done by applying the Navier-Stokes equations for compressible flows. The governing equations have been used as follows [48,53]:

a) Continuity equation

$$\frac{\partial \rho}{\partial t} + \frac{\partial}{\partial x_i}(\rho u_i) = 0 \tag{2}$$

Momentum equation

$$\frac{\partial}{\partial t}(\rho u_i) + \frac{\partial}{\partial x_j}(\rho u_i u_j) = \frac{\partial}{\partial x_j}\left[-P\delta_{ij} + (\rho u_i) + \mu\left(\frac{\rho u_i}{\rho x_j} + \frac{\rho u_j}{\rho x_i}\right)\right] + f \tag{3}$$

where ρ, t, u_i, u_j, x_i, and x_j represent the gas flow density, the time and velocity, and spatial coordinate in the related direction, respectively. μ denotes the dynamic viscosity, P represents the force exerted by pressure differences within the fluid, and f summarizes any external forces. For closing those equations, RANS (Reynolds Averaged Navier Stokes) - turbulence models have been used in literature considering mean flow quantities only and therefore reducing the computational costs [53]. For CGS applications, the k-ε model is widely used in literature [14,33]. Since this model provides weaknesses close to the wall, the k-ω SST (Shear Stress Transport) model was applied within this work using blending functions for the transition from near-wall to far-field zone [54]. For solving the fluid-phase flow field problem, the turbulence kinetic energy (k) and specific dissipation rate (ω) can been obtained from equations Eqs. (4) and (5) [55]:

$$\frac{\partial}{\partial t}(\rho k) + \frac{\partial}{\partial x_i}(\rho k u_i) = \frac{\partial}{\partial x_j}\left[\Gamma_k \frac{\partial k}{\partial x_j}\right] + G_k - Y_k + S_k \tag{4}$$

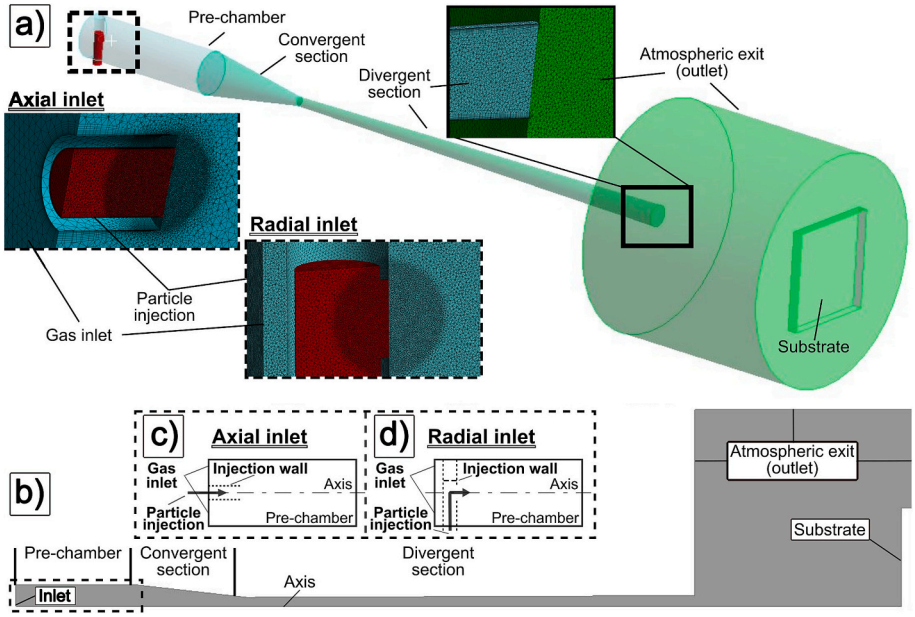

Fig. 3. For the three-dimensional computational domain in ANSYS (a), a schematic cross sectional model domain illustrates the boundaries (b). All geometries have the same structure with inlet, pre-chamber, convergent – divergent nozzle section and outlet plus substrate if necessary. An axial (c) and a radial particle inlet (d) have been investigated.

$$\frac{\partial}{\partial t}(\rho\omega)+\frac{\partial}{\partial x_i}(\rho\omega u_i)=\frac{\partial}{\partial x_j}\left[\Gamma_\omega\frac{\partial\omega}{\partial x_j}\right]+G_\omega-Y_\omega+D_\omega+S_\omega \tag{5}$$

where G represents the generation of k and ω due to mean velocity gradients, respectively, Γ represents the effective diffusivity of k and ω, respectively. Y represents the dissipation of k and ω in the turbulence and S are user-defined source terms with D_ω as cross-diffusion term. A modified formulation is utilized in ANSYS Fluent [56]. Nitrogen has been considered as ideal gas.

Lagrangian method has been used for computation of the particle phase, resulting in the following force balance [57]:

$$m_p\frac{dv}{dt}=F_D+\overrightarrow{F}_{other} \tag{6}$$

where m_p is the particle mass, v the particle velocity and F_{other} represents further external forces, e.g. gravity or Saffman force which have all been neglected based on previous testing of the model. Particles have been considered as spherical, the drag force F_D was obtained by applying the 'high-Mach-number' relation, which is a modified version of the model proposed by Morsi and Alexander [58]:

$$F_D=\frac{1}{2}C_D\rho_g(u-v)^2A_p \tag{7}$$

where C_D is the drag coefficient, ρ_g is the fluid density and A_p is the projected area of the particles. The discrete random walk model has been applied to take the dispersion within a turbulent flow into account. To consider varying fluid velocities in the radial direction within the de Laval nozzle, the spinning effect of spherical particles has been additionally introduced by applying the so-called Magnus effect. The resulting lift force can be obtained as follows [35]:

$$F_L=C_L\frac{1}{2}\rho_g(u-v)^2A_p \tag{8}$$

where C_L is the lift coefficient. Since several models for this lift coefficient are available, preliminary studies have been carried out modeling the spray spot size. Based on these results, the model of Rubinow and Keller [59] was selected to evaluate the lift coefficient.

Particle size distribution of the powder was modeled in ANSYS Fluent using the Rosin-Rammler distribution:

$$Y_d=e^{\left(-(d/\bar{d})^n\right)} \tag{9}$$

which is an exponential relationship between the mass fraction Y_d and the corresponding specific particle diameter d. The mean diameter $\bar{d}$ ($d_{50}=14$ µm) and spread parameter $n=4.35$ have been obtained from previous studies using the same powder by Singh et al. [25].

4. Results and discussion

4.1. Particle velocity for axial and radial particle injection

One objective of the actual study was to investigate the effect of the selected particle injection type. An axial injection and a radial injection were employed in the computational model in order to facilitate a comparison of two distinct applications for powder injection [45,48]. The latter represents the radial injection in the applied Impact 5/11 cold spray facility for the actual study. The computational results of both types of injection (indicated by subscript 'M') were compared to results of the in-flight diagnostics at the appropriate spray distance of 60 mm. The HiWatch HR2 generates a 'cloud of datapoints' within the designated measurement area, whereas the CSM focuses on the point within the particle beam exhibiting the highest detection rate. Since Out1 has already been used extensively in previous studies [11,41,49], the initial investigations relate to this nozzle.

The results of the particle velocity for Out1 from the CFD model and diagnostics in the lateral distance are illustrated in Fig. 4. The HiWatch 'cloud of datapoints' was fitted using the method of least squares. The same procedure has been conducted for the CFD results, where the particle data have been obtained from a representative layer for the substrate. Here, the HiWatch revealed a parabolic-shaped contour of the particle velocity with the highest speed (approx. 875 m/s) in the spray direction located at the center and lowest at the edge region. The CSM measurement, focused on the centroid point within the plume, verifies those results with an average velocity of approximately 886 m/s at the centroid point. The experimentally obtained particle velocity revealed a near-symmetrical distribution of particle velocity over the lateral distance, where an excessive drop towards the upside view was observed

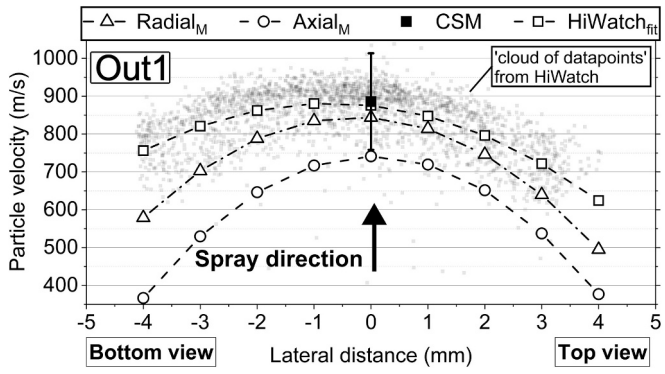

Fig. 4. The particle velocity of Out1 over lateral (= vertical) distance, measured via HiWatch (empty squares), has been fitted for improved visibility and compared to the CSM (full square) measurement. The direction of the spray plume is indicated by the large arrow. The fitted plots for the radial (empty triangles) and axial (empty circles) injection are displayed for the CFD model, denoted by the subscript `M`. Error bars are only indicated for the CSM with reference to Table 3.

($\Delta v_{edge,HjWatch} \approx 130$ m/s). It is therefore assumed that the particles are accelerated and dispersed inhomogeneously within the nozzle. This can also be observed from the total number of detected particles in the lateral distance. In particular, towards the positive lateral direction, the particle density has decreased rapidly.

The axial and radial particle injection were aligned with the parabolic HiWatch contour, incorporating an offset for the obtained velocity magnitude. The radial injection revealed the larger velocity close to the experimental data in the center while causing a decreased particle velocity at the edges of the spray plume. The axial injection yields a significantly lower maximum particle velocity ($\Delta v_{max,rad\text{-}ax} \approx 100$ m/s) and a continuous offset over the lateral direction. While the axial injection reveals a symmetric velocity distribution, the edge velocity of the radial injection differs ($\Delta v_{edge,rad} \approx 80$ m/s, $\Delta v_{edge,ax} \approx 10$ m/s). The velocity data at the centroid of the plume is summarized in Table 3. It should be noted, that an additional calculation in ANSYS with activated gravity effect didn't result in any significant changes. It is therefore assumed that the decrease in vertical particle velocity is a result from the gas properties of the particle injection, yielding a characteristic, biased particle distribution. The difference in particle velocity at the center was attributed to the injection type as well, which will be elaborated further below.

Fig. 5 illustrates the contours of velocity, viscosity and temperature for the modeled axial and radial injection within the pre-chamber. In the case of axial injection within the pre-chamber, a substantial two-phase region with a cold core, resulting from the combination of a hot propellant and a cold carrier gas, can be observed. The two contours are oriented towards the convergent nozzle section due to the same orientation along the axis yielding a separated temperature zone (Fig. 5a). In the case of radial injection, the two gas flows are mixed immediately behind the injection point, resulting in a more diffusive contour due to the differing inlet directions and the perpendicular placement of the tube, which impedes the surrounding propellant gas flow.

Turbulence in the form of eddies is expected to occur within this diffusive zone, where the turbulent kinetic energy is typically higher than in the non-diffusive zone resulting from axial injection [53]. Such effects can result in enhanced mixing, causing a more uniform distribution of gas properties in the radial direction due to an increased rate of momentum transfer across the flow. The consequences of mixture were most evident in the viscosity of the pre-chamber, as illustrated in Fig. 5b, where a combination of cold carrier gas and hot propellant gas was observed. This trend was observed to persist throughout the entire length of the nozzle, as demonstrated by the axial profiles.

Moreover, the mixed hot gas from the radial injection exhibits a more extensive expansion, exhibiting a better-distributed viscosity in the radial direction. It was therefore proposed that the more pronounced gas expansion will result in an enhanced gas velocity for the radial injection. A comparison of the velocity profiles for both injection types reveals that the overall velocity is similar for radial and axial injection in the subsonic, convergent section (Fig. 5c). Subsequently, the gas flow transitions into the supersonic regime, where compressibility effects become apparent. In addition to the reduced temperature observed for the axial injection, the less pronounced mixing of cold carrier gas and hot propellant gas results in a deceleration of the overall flow due to effects such as internal friction and thus reduced particle velocity.

Table 3
Modeled and measured velocity at the centroid point of the plume for Out1.

Lat. Distance = 0 mm	Axial	Radial	HiWatch	CSM
Velocity [m/s]	741 ± 82	843 ± 109	875 ± 103	886 ± 127

4.2. Modeled and experimental spot profiles

One primary goal of this study is to validate spray profiles based on the modeled data in ANSYS. The three-dimensional model with radial injection was applied due to the better agreement with the in-flight particle analyses. In order to facilitate a comparison between the width of the (typically) spherical spray spot and the positional data obtained from the substrate boundary at a spray distance of 60 mm in the CFD model, line profiles have been created using the sprayed data. A negligible proportion of the modeled particles did not reach the requisite critical velocity and were therefore excluded from the analysis [19]. The complete procedure is illustrated in Fig. 6.

First, a line profile was created using Out1, as described in the 'Material and methods ' – section, under equal spraying conditions (Fig. 6a). The measured profile width was approximately 8 mm with the topographical analysis indicating a Gaussian profile [26]. Given the presence of scattered particles in the edge area and the difficulty in distinguishing the initial stages of the profile build-up from the substrate, a transition area based on a threshold has been established. In Fig. 6b, the cross-section of three line profiles has been transferred into a Gaussian fit and displayed normalized to the maximum value (Eq. (10)).

$$y = y_0 + Amp^{*}\exp\left(-\frac{(x-x_0)^2}{2w^2}\right) \tag{10}$$

where y_0 and x_0 are the offset in the vertical and horizontal direction, *Amp* is the amplitude, and *w* the standard deviation of the fitting curve. Considering a threshold of 5 %, the profile width was estimated to be 4.4 mm. Based on previous experiments, the as-sprayed spray spot is considered circular shaped. On that background, the line profile width has been transferred into an ideal, circular-shaped spray spot with the diameter extracted from the fitted profile in Fig. 6c.

Particles with equal properties and size distribution have been implemented into the ANSYS model. The impact position of the modeled particles obtained from the substrate boundary is given in Fig. 6d. It can be observed that there is a vertical bias in the particle distribution resulting in an oval-shaped distribution. This might be an artifact of the gas flow properties due to the radial injection, which will be discussed later. To create a height profile of the spot, this cumulative distribution must be transferred into a volumetric one based on the specific particle diameter, as large particles are expected to be located in the center and contribute more to the profile build-up (Eq. (11)).

$$N_p = \frac{V_p}{V_{p,total}} \tag{11}$$

where N_p is the relative amount of each particle with volume V_p related to the total volume $V_{p,total}$. This approach results in several bars

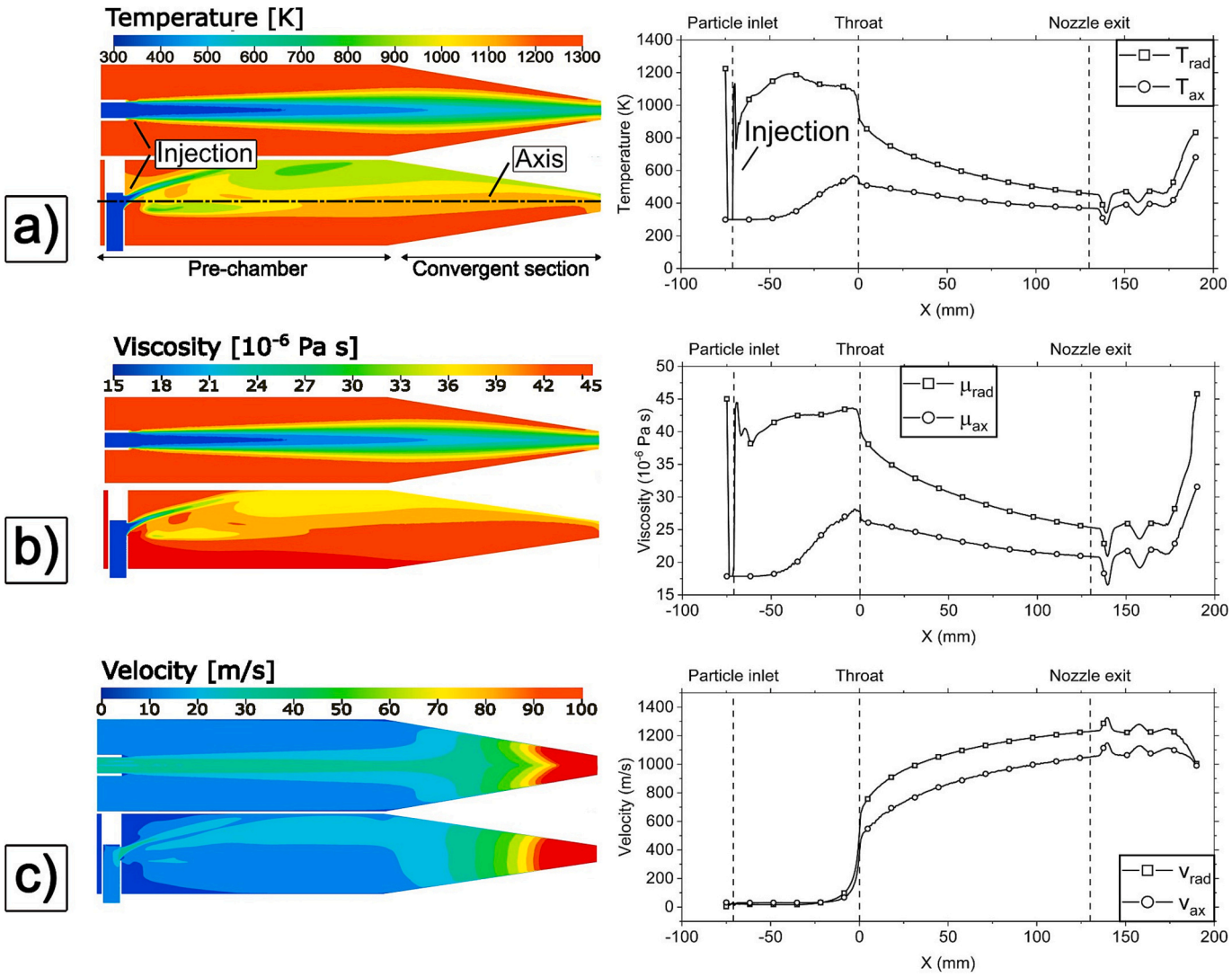

Fig. 5. Modeled temperature (a), viscosity (b) and velocity (c) contour plots of the gas for axial (top) and radial (bottom) injection, respectively, are given on the left hand side. The corresponding axial profiles are displayed on the right hand side.

depending on the particle volume within the chosen step size of 1 mm, as shown in Fig. 6e. Here, the size distribution is given in y direction over the z direction. In contrast to the cumulative distribution, the profile now exhibits a less biased distribution in y direction. Small particles were no longer given as much consideration. By considering both in-plane directions, a matrix based on the deposited particles sizes in both directions can be obtained. The resulting spray profile has now been modified to align more closely with the anticipated spray profile, and is displayed normalized on the maximum value (Fig. 6f). In the region of the image indicated by the dark blue colour, scattered elevations can still be identified, which correspond to the area below the specified threshold value. Starting from the first large orange contour representing the threshold, a diameter of 9.3 mm in the z direction (d_z) and 11.9 mm in the y direction (d_y) can be approximated. In order to obtain an initial estimate of the diameter from the ideal, circular-shaped spot, the equal area for the elliptical area on the ground was considered. Such an approach yields a calculated diameter of ~10,5 mm, which was slightly larger than the experimental value of 8.8 mm but still in good agreement.

Based on the procedure in Fig. 6, spray spots for the axial injection as well as the radial injection without applied lift model have been computed. The volume of the simulated particle profiles was kept constant since the same amount of particles has been applied. The axial injection in Fig. 7a results in a thin, sharp and symmetric profile, whose diameter was not consistent with the experimentally achieved spray spot. A slightly increased scattering of particles has been obtained by applying the Lift model (Fig. 7b). The correlation between the experimental profile and the observed outcome remains unsatisfactory. In Fig. 7c, the pure radial injection results in a larger but non-symmetric spot profile. The particles exhibit a biased distribution in vertical direction but less pronounced in comparison to the previous achieved results. However, the diameter of the modeled profile is still significantly smaller in comparison to the experimental data. In contrast to studies on CGS spray spots conducted under less harsh conditions with a radial injection [48], the employment of the Lift model was necessary for an accurate particle dispersion in the actual study.

In the context of the particle dispersion, a biased distribution of the velocity along the y-direction was observed for the radial injection. One reason for this biased distribution might be a considerable sensitivity of the gas properties and flow patterns to the radial injection, which is also inserted in y-direction into the pre-chamber. Fig. 8a illustrates the velocity contour over the axial distance x within the nozzle. The propellant gas flow carrying the principal amount of gas through the nozzle gets divided right in the beginning by the perpendicular implemented injector in z-direction. This results in a non-symmetrical gas flow (Fig. 8b), which is in contrast to the axial injection [14]. Upon

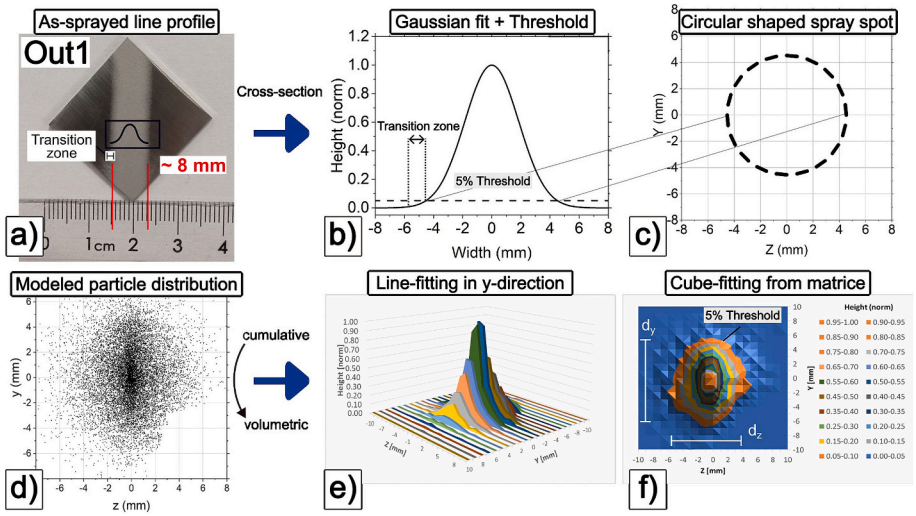

Fig. 6. The as-sprayed line profile from Out1 (a) is transformed into a cross-sectional profile by means of topographical analysis (b). A Gaussian fit was applied over three of such profiles. A circular spray profile was extracted based on the applied threshold (c). The cumulative particle distribution modeled in ANSYS (d) was converted into a volumetric distribution. A height profile can be obtained by adding fitting bars at a step size of 1 mm in y direction (e). By considering both in-plane directions (visible at the squares), a two-dimensional contour mapping illustrates the spray spot (f, 5 %-threshold at the large orange zone).

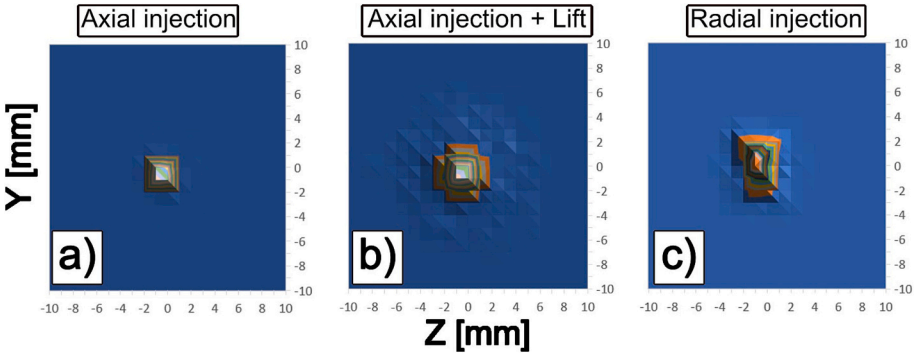

Fig. 7. Simulated spray spots as 2D contour plot (referenced to Fig. 6**f**) for the axial injection with (a) and without Lift (b) as well as the radial injection without Lift (c). All profiles have been normalized on their respective maximal height value.

reunification of the gas flow behind the injector prior to its entry into the convergent nozzle section, a rise in pressure is observed along the y axis, resulting in an enhanced velocity (Fig. 8c). After passing the throat and reaching the supersonic region, the biased velocity distribution is still present within the divergent section of the nozzle. An elliptical-shaped velocity contour is formed instead of the symmetrical, circular-shaped one, matching the modeled spray spot results (Fig. 8d). It is therefore assumed that the particles follow the initial pressure and velocity gradient, resulting in a biased distribution along the y-direction.

4.3. Comparison of different nozzle geometries

The expansion ratio and the length of the divergent nozzle are considered as key factors for the evolving gas velocity and temperature [60]. Furthermore, the influence of the applied particle injection could be demonstrated. These results for Out1 were transferred to two other commercial nozzle designs in cold gas spraying systems. As given in the section 'Cold spray setup', the nozzle variant Out4 has a longer divergent part and a larger exit diameter. Such a geometry is expected to yield larger gas velocities at a decreased temperature. This effect is likely to be more pronounced for the nozzle Out2, which is shorter but exhibits a considerably larger expansion ratio. Given the substantial increase in the expansion ratio, the decline in gas temperature and the acceleration of the gas velocity may be even more pronounced in comparison to Out4. All nozzle geometries are of identical dimensions with respect to the prechamber, the convergent section and the radial injection.

The gas velocity and temperature of Out1 are illustrated in Fig. 9a at the exit of the divergent nozzle section. There is an 'under-expanded' flow visible since the pressure of the fluid towards the nozzle exit is higher than the ambient pressure [61]. Thus, the gas flow expands to a small extend right after leaving the nozzle. The shock-diamond structure tends to decrease the kinetic energy of the gas flow, resulting in a slightly smaller gas velocity. It should be noted that no significant effect from the shock diamonds on the general particle velocity was observed. It is assumed that this effect is a consequence of the size and density of the IN718 particles. Out4 reveals a well-fitting flow structure after the nozzle exit (Fig. 9b); in literature, this is marked as 'correctly-expanded' for a matching exit and ambient pressure [61]. An increased gas velocity could be observed for Out4 in comparison to Out1, although the absolute differences between the nozzles are small overall. The gas flow of Out2 is characterized by an 'over-expanded' state, in which the gas pressure falls below the ambient pressure due to the extensive cross-sectional expansion (Fig. 9c). Hence, the flow starts to form the shock diamond structure within the divergent nozzle part already. The large expansion ratio also yields the highest gas velocity for Out2, regardless of the distinctive shock diamond structure. The difference in gas properties was particularly evident in relation to the temperature. The high gas velocity in Out2 is accompanied by a significant reduction in the gas

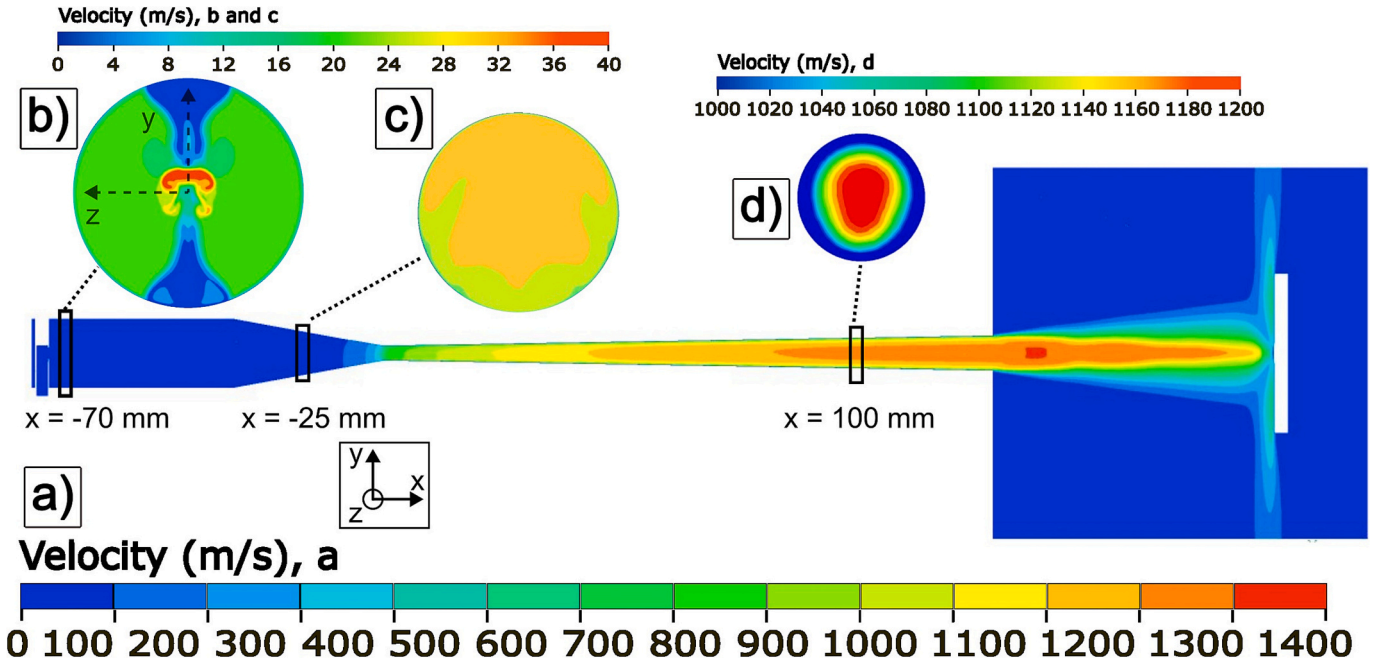

Fig. 8. Cross section of the velocity contour (a) from Out1 within the pre-chamber (b), the convergent section (c) and the divergent section (d). The axial distance was referred to the throat at x = 0 mm. The scale bar has been adjusted per plot (0–40 m/s for b and c, 1000–1200 m/s for d) to illustrate the variation in velocity.

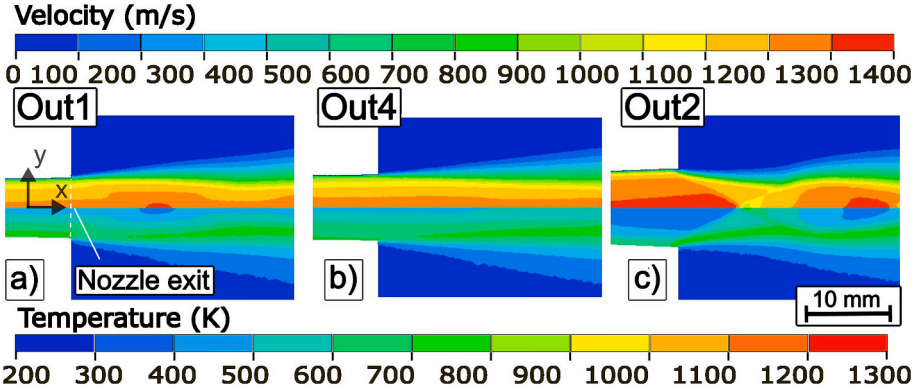

Fig. 9. Velocity (top) and temperature (bottom) contour plots at the nozzle exit for the three nozzle geometries Out1 (a), Out4 (b), and Out2 (c).

temperature due to the more pronounced gas expansion. Out4 also revealed a decreased gas temperature but to a smaller extend due to the increased divergent nozzle section. This provides further evidence to support the argument that Out4 can be considered a quasi-extension of Out1. The gas properties at the nozzle exit is summarized in Table 4.

The respective particle data for each nozzle is exemplary given in the same table for an IN718 particle with mean diameter (d_{50} = 14 µm). A reduced particle temperature and increased particle velocity could be observed for Out4 in comparison to Out1. In contrast to the assumptions based on the properties of the gas, Out2 has a lower particle velocity and a higher particle temperature. It is therefore assumed that the large expansion ratio cools the gas rapidly, while the brief divergent section does not provide sufficient time for the particles to be affected by the cold gas. To estimate the change in particle temperature over time in a supersonic flow within a divergent nozzle section, an energy balance approach can be applied. By assuming a uniform particle temperature due to the high thermal conductivity of the sprayed metal powder, the heat transfer between gas and particle was assumed to be governed by the following, simplified equation [33,62]:

$$\frac{dT_p}{dt} = \frac{hA_p}{m_p\, c_p}\left(T_g - T_p\right) \tag{12}$$

where dT_p/dt refers of the of change of particle temperature over time and h to the convective heat transfer coefficient. A_p, m_p and c_p describe the projected area, mass and specific heat capacity of the particle, respectively. T_g is considered as the corresponding recovery temperature for the boundary layer surrounding the particle [33]. The convective heat transfer coefficient can be assumed to be primarily determined by the heat conductivity of the gas, which behaves like the gas temperature. As observed above, the gas temperature for Out2 is considerably lower compared to the other ones due to the large expansion ratio.

Table 4
Gas data, obtained by applying an axial line, and particle data, obtained by inserting a single IN718 particle with mean diameter, at the nozzle exit for all three geometries, respectively.

Nozzle exit data	v_g [m/s]	v_p [m/s]	T_g [°C]	T_p [°C]	p_g [MPa]	t_{div} [ms]
$Out1_{exit}$	1200	706	200	561	0.130	0.19
$Out2_{exit}$	1286	631	76	591	0.045	0.14
$Out4_{exit}$	1229	769	175	525	0.103	0.24

It can be therefore be assumed that the change in particle temperature is lower per time increment and thus yields higher particle temperatures at the nozzle exit. The respective time increment is considered as the dwell time of a particle in the divergent nozzle section. Due to the short time period of a particle within this region of Out2, the change in particle temperature is also smaller. An analytical estimation was then conducted by applying the following simple relationship, which did not consider factors such as particle bouncing from the nozzle walls:

$$dt \approx \Delta t_{div} = \frac{v_{p,exit} - v_p^*}{L_{div}} \quad (13)$$

In Eq. (13), the interaction time Δt_{div} results from the difference in particle velocity at nozzle exit $v_{p,exit}$ and throat v^*_p, divided by the length of the divergent nozzle section L_{div}. The results for all three nozzles are presented in Table 4. Out2 exhibits the lowest interaction time within the nozzle, indicating the short time period for gas-particle interaction. Out4, which is a quasi-extension of Out1, revealed an increased interaction time. These findings combined with the assumptions for the expansion ration support the hypotheses regarding the anomalous properties of the gas and particles observed in Out2.

In the following step, experiments have been conducted for the particle velocity and spray profiles of the two other nozzles. Once more, fitting functions have been extracted from the HiWatch measurement as well as line profiles of Out2 and Out4. In the CFD model, particles have been injected in the same way as performed for the spray profile of Out1. The spray profiles were then normalized using the data from Out1 as a reference.

The modeled velocity profiles of the particles are given in Fig. 10a in comparison with the experimentally obtained results. First, it can be noted that the order of measurement and modeling for the particle velocity profile agree with the results obtained from the nozzle exit ($v_{p,Out4} > v_{p,Out1} > v_{p,Out2}$, Table 4). In comparison to the results for pure axial and radial injection, the additional Lift model yields a velocity in the radial direction that is less parabola-shaped with a decreased maximum velocity but consistent order of the nozzle geometry. It is important to highlight that the profiles of nozzles Out2 and Out4 without lift are consistent with those of purely radial particle injection regarding the same order.

Fig. 10b illustrates the Gaussian spray profiles for the three geometries normalized to the maximum height of Out1. The experimentally obtained spray profile from each nozzle has been analyzed accordingly to the procedure in Fig. 6. All nozzles demonstrated a deposition efficiency that fell within a similar range. The profile for Out4 was higher and slightly wider than Out1. Those spray profiles were relatively sharp in contrast to Out2, where the height of the profile is smaller but its width is significantly expanded compared to the other two ($Amp_{Out4} > Amp_{Out1} > Amp_{Out2}$). The threshold is the same for all three geometries (5 %). The corresponding spot diameters are given in Table 5.

The volumetric particle distribution obtained by the ANSYS model is shown in Fig. 10c-e for each nozzle. The ground is marked by a sparse pattern and the threshold by a pink line. In contrast to the first results, where the step size of the fitting was included, those plots focus on the three-dimensional contour at equal step size with a smoother shape for improved visualization of each profile. The profiles of Out1 and Out4 are generally very similar. However, the diameter of Out4 is slightly larger, which aligns with the experimental result. As the same particle volume was used in the simulation, the absolute profile height is lower than that of Out1, although the maximum height should be higher based on the

Table 5
Extracted diameter of the circular fit for model and width of the line profile by applying the threshold of 5 %. The area of an ellipsoid has been transferred into a circle to obtain the radius/diameter.

Spot diameter		Out1	Out2	Out4
Modeled	[*mm*]	10.52	12.64	10.87
As-sprayed	[*mm*]	8.80	10.00	9.20

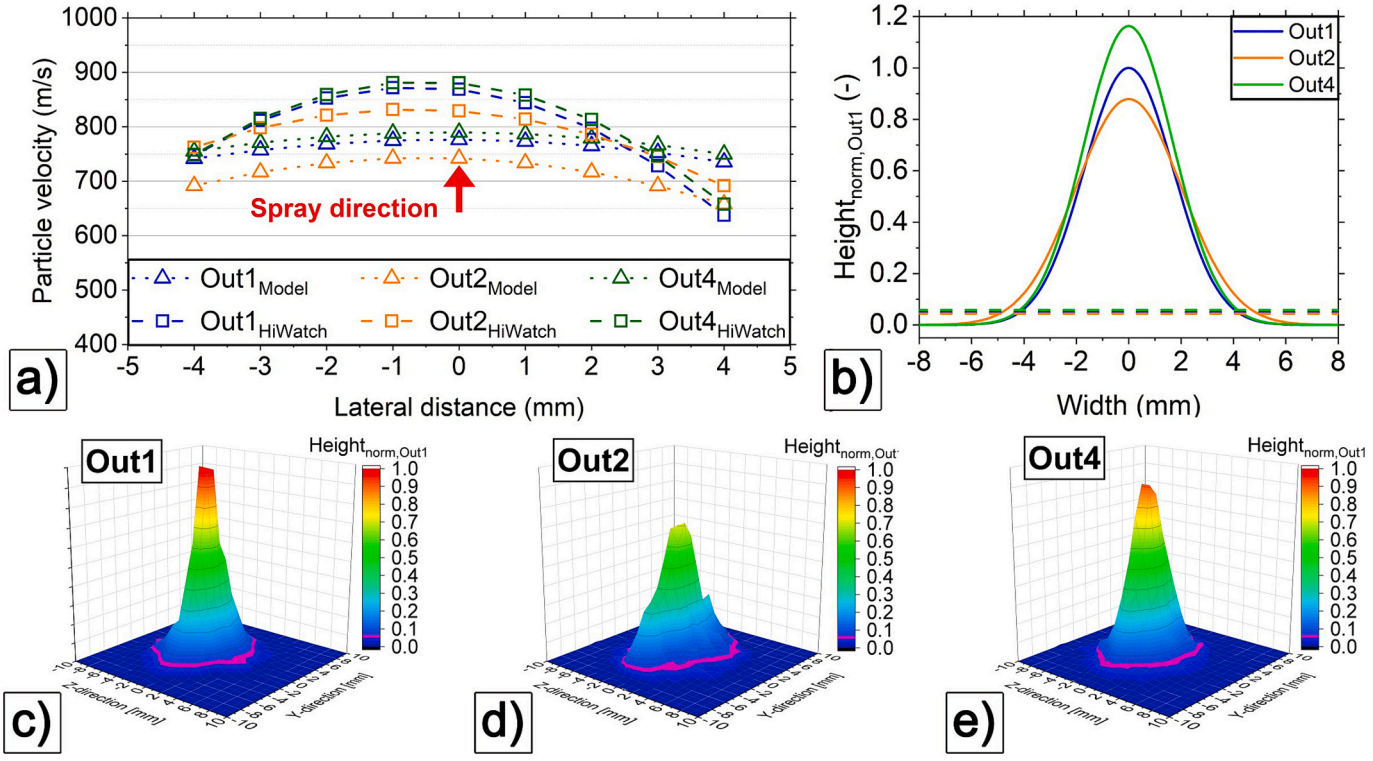

Fig. 10. The modeled (triangles) and measured (squares) velocity profiles in vertical direction (a) have been compared for Out1 (blue), Out2 (orange) and Out4 (green). Gaussian fits of the as-sprayed profiles for those geometries are illustrated with their specific threshold, normalized to Out1 (b). Three-dimensional contour plots of each spray spot have been obtained from the modeled data in ANSYS (c-e, threshold in pink).

spray profiles. This indicates that the equation used for the critical velocity cannot fully reflect the actual deposition efficiency. Additionally, there is an increased number of scattered particles around the actual spray spot. In agreement with the as-sprayed samples, the modeled Out2 profile revealed a broad particle distribution at decreased height ($Amp_{M,Out1} \geq Amp_{M,Out4} > Amp_{M,Out2}$) but increased width compared to the other longer nozzles ($d_{M,Out2} > d_{M,Out4} \geq d_{M,Out1}$). It can be generally asserted that the spot size was in a strong correlation with the diameter of the nozzle exit.

4.4. Residual stress analysis for each nozzle geometry

Based on the measured results, the residual stress state was analyzed since this is considered as critical for the spraying process. Out1 has been applied in previous studies using the same materials and revealed good results for DE, density and adhesion [41,49,63]. As observed above, the flow for Out4 yielded a smother gas flow contour. On the other hand, the increased velocity at slightly lower temperature might increase the peening effect and therefore the compressive residual stress even further. This might differ for Out2, where the particles reach the nozzle exit at still elevated temperatures but relatively low gas temperatures.

Fig. 11 visualizes the ICP results for the three different nozzles. Each run consists of three pre-heating cycles (moving the gun without powder injection), followed by eight subsequent deposition cycles and the cooling period. The coating thickness has revealed to be 698 ± 15 µm, indicating no significant change in DE of approximately 80 %, as demonstrated by experiments using the same setup [41]. The negative increase in curvature in Fig. 11a represents an increasing compressive residual stress state during the deposition process. For each nozzle, the subsequent impact of solid particles yields peening stresses, which are compressive in nature and dominant in CGS. Out1 revealed the most minor change during the deposition compared to the other two ($\Delta\kappa_{Out1} = 0.13\ m^{-1}$, $\Delta\kappa_{Out2} \sim \Delta\kappa_{Out4} = 0.19\ m^{-1}$), whose shapes were in good agreement. No significant, permanent change in curvature after the pre-heating cycles could be observed. Out1 and Out4 revealed a consistent trend during the cooling period with respect to the offset in curvature. In contrast, Out2 reached the constant curvature value faster. Consequently, it was assumed that a smaller thermal gradient between the coating and the substrate would result from the impingement of cold propellant gas.

This assumption was further investigated by applying the analytical model for estimating the thermal gradient from various surface scanning speeds, as described in our previous study [41]. It is necessary to make certain modified assumptions in advance. The particle velocity could not be assumed to be constant anymore as shown already. This also affects the spray spot size, which correlates with the size of the nozzle exit. The temperature at the rear of the substrate was approximately 130 °C for all three nozzles. A significant change in substrate temperature was only obtained for the changed scanning speed. Material data and spray distance have been applied consistently. To calculate the local temperature on the impact zone, the modeled temperature from gas and d_{50}-particle at the substrate boundary have been extracted (see Table 6). The local temperature is directly correlated with the thermal gradient that forms after the nozzle traverses a specific area. This thermal gradient is subsequently balanced, resulting in tensile residual stress that counteracts the compressive residual stress induced by particle impact. Due to the limitations of the model, which cannot yet handle varying particle velocities, the analysis was limited to the developing thermal gradient.

The presented results relate to individual measuring points and serve as an approximation to describe the processes in the context of a scale effect. In general, the temperature data obtained from the substrate correlates with that of the nozzle outlet. Out2 results again in the lowest gas temperature and highest particle temperature. This was accompanied by the largest spot size, which is significantly larger than that of the other two nozzles. As the volumetric profiles are nominated, the crucial part is the spot diameter. Hence, Out2 yields the lowest ratio of induced heat per unit area. In conjunction with the cold gases, this effect appears to counteract the impact of the warmer particles, resulting in a relatively small thermal gradient. The hereby resulting tensile residual stresses balance the dominant compressive residual stresses to a lesser extent, which is in turn consistent with the observations obtained from the ICP sensor for Out2.

It is therefore proposed that the larger thermal gradient present in the other nozzles serves to counteract the dominant compressive stresses to a greater extent. The thermal gradient has been identified as the smallest for Out2 at a close range to Out4, while the latter presented an improved ratio of heat per area unit. Both nozzles yielded a large compressive residual stress state to a larger extent for Out2 (see Fig. 11b). Although the peening effect is expected to be lower due to the slower and warmer particles, it would appear that the lower thermal gradient in the impact zone is the decisive factor. The general change in

Table 6
The local temperature per geometry was calculated according to Eq. (10) and the given material parameter in our related study [41]. In addition to the spot size data from Table 5, the measured substrate temperature was applied, which was approximately 130 °C for all three nozzles.

Substrate data		Out1	Out2	Out4
T_g	*[K]*	1259	1244	1253
T_p	*[K]*	790	803	715
T_{loc}	*[K]*	462	457	458

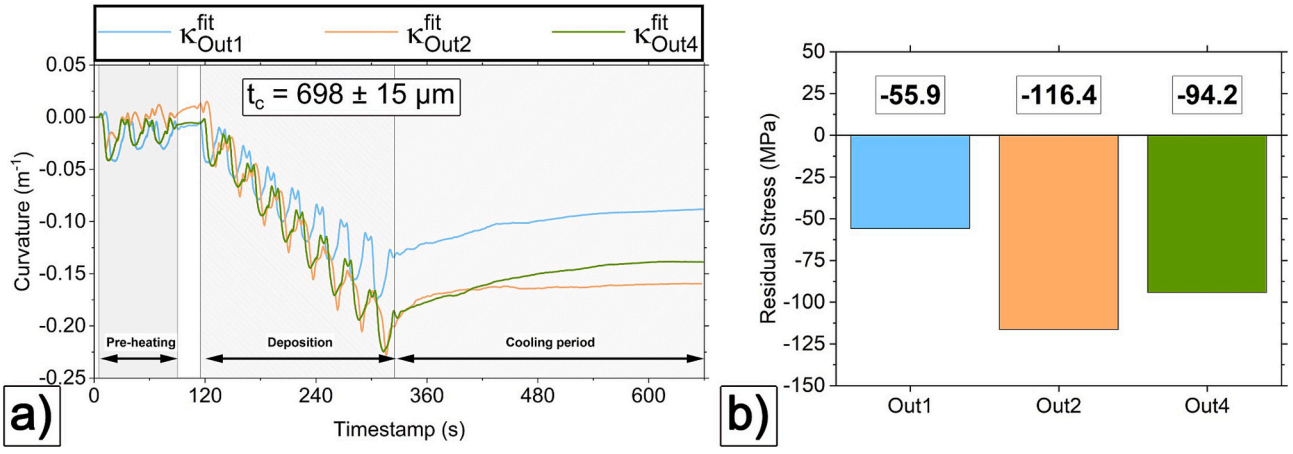

Fig. 11. Residual stress results from the in-situ curvature for Out1, Out2, and Out4. The curvature is plotted as a fitted version for improved visibility (a). The corresponding residual stresses for each nozzle are illustrated as well (b).

curvature during the cooling phase indicates the presence of tensile thermal stresses. Based on the assumption of equal material properties, the curvature reaches a constant value more rapidly for Out2. This phenomenon can be attributed to the previously observed overall low process temperature for this nozzle. For Out4, the relatively similar local temperature and curvature change during the cooling period indicates similar process temperatures to Out1. It is therefore assumed that the overall largest process temperature, smallest spot diameter and moderate particle velocity yield the lowest compressive residual stresses as observed from the in-situ curvature measurement.

It is important to note that the CFD simulations and analytical modeling presented in this study represent a simplified approach of the actual CGS process. In light of the considerations presented earlier, the modeled outcomes demonstrated a satisfactory correlation with the experimental findings. The simulation results presented should be regarded as preliminary indications, as the results along the axis and for individual particles are still subject to a scale effect. In addition to the diagnostic data presented, measurements of the particle temperature would also provide further insights. Against this background, the CFD model has already shown reliable results. It should be noted that the data presented are subject to fluctuations that the CFD model is unable to fully reproduce. In addition to the scale effect, this is particularly relevant in the context of particle dispersion against the background of particle injection, given the present operating parameters of the CGS system. A close match has been demonstrated between the lift model and the experimentally determined spray profiles. Further investigations have to be carried out to examine the influence of such models on the particle properties and the interaction with the gas jet. From these results, it can be expected that an axial injection at the applied facility will reduce the size of the spray spot. Furthermore, more residual stress analyses, also by means of other analyses methods such as the incremental hole drilling method, have to be conducted for further validation of the achieved results and even more precise modeling.

5. Conclusions

The objective of this study was to investigate the particle trajectory and dispersion during cold gas spraying of IN718 powder at elevated gas conditions. A three-dimensional CFD model was implemented using ANSYS Fluent with a focus on particle injection and dispersion. In contrast to the simplified, axisymmetric model, a radial injection was introduced to match the actual setup of the cold spray equipment used. The modeled particle velocity has been validated with in-flight particle diagnostics using the HiWatch and CSM diagnostic systems. Spray experiments on three different nozzle geometries were performed and compared with the predicted data obtained from the computational model. A simplified approach converting simulated particle data into a volumetric spray profile was presented. The ICP sensor residual stress results for all nozzle geometries were discussed based on the modeled data. The main conclusions are as follows:

- The in-flight particle velocity diagnostics for IN718 particles, using the HiWatch and CSM systems, has provided consistently accurate velocities. The CFD simulation for radial instead of axial particle injection showed a good agreement between the modeled and experimental particle velocities. This validates the model.
- A simplified procedure for the generating volumetric spray profiles based on modeled particle distributions was presented. The modeled spot size was found to be in good agreement with the as-sprayed spot profiles, indicating that an additional lift model is necessary for accurate results. A significant sensitivity to the injection type was observed in the modeling results, indicating that an axial injection could significantly narrow the spray spot in the spray facility used. This can be a helpful effect for applications of cold spraying for repair or additive manufacturing.
- The experimental results from three different nozzles are in good agreement with the simulated results for the spray spot size. For each nozzle geometry, the particle trajectory and therefore the spray spot size correlates with the diameter of the divergent nozzle exit. This allows the spray spot size to be adjusted in a targeted manner.
- Residual stress analyses for the different nozzle geometries were performed using in-situ curvature measurement. The gas temperature and velocity, which are determined by the respective divergent nozzle section, influence the resulting residual stress state. An increased expansion ratio results in higher compressive residual stresses. Furthermore, the CFD model showed that also warmer particles resulted in increased compressive residual stresses and a wider spray spot, particularly in scenarios with a shorter divergent nozzle section at high expansion ratios. These findings enable the targeted adjustment of residual stress states in cold sprayed coatings.

Credit authorship contribution statement

J. Schmitt: Methodology, Conceptualization, Writing – original draft, Formal analysis, Writing – review & editing, Visualization, Data curation. **G. Mauer:** Writing – review & editing, Methodology, Validation. **R. Mücke:** Validation, Methodology, Software, Writing – review & editing, Data curation. **J. Fiebig:** Methodology, Writing – review & editing. **O. Guillon:** Resources, Supervision. **R. Vaßen:** Supervision, Funding acquisition, Resources, Writing – review & editing, Project administration.

Declaration of Generative AI and AI-assisted technologies in the writing process

During the preparation of this work the author(s) used DeepL in order to improve the readability and language of the manuscript. After using this tool/service, the author(s) reviewed and edited the content as needed and take(s) full responsibility for the content of the published article.

Declaration of competing interest

The authors declare that they have no known competing financial interests or personal relationships that could have appeared to influence the work reported in this paper.

Acknowledgements

The authors acknowledge the financial support by the German Research Foundation (DFG) under grant number VA163/11-1. Special thanks to Mr. Karl-Heinz Rauwald for his help to operate the cold spray facility.

Data availability

Data will be made available on request.

References

[1] A.P. Alkhimov, A.N. Papyrin, V.F. Kosarev, N.I. Nesterovic, Gas-Dynamic Spraying Method for Applying a Coating, 5,302,414, n.d.
[2] M.B. Henderson, D. Arrell, R. Larsson, M. Heobel, G. Marchant, Nickel based superalloy welding practices for industrial gas turbine applications, Sci. Technol. Weld. Join. 9 (2004) 13–21, https://doi.org/10.1179/136217104225017099.
[3] T. Petrat, B. Graf, A. Gumenyuk, M. Rethmeier, Laser metal deposition as repair technology for a gas turbine burner made of Inconel 718, Phys. Procedia 83 (2016) 761–768, https://doi.org/10.1016/j.phpro.2016.08.078.
[4] T. Suhonen, T. Varis, S. Dosta, M. Torrell, J.M. Guilemany, Residual stress development in cold sprayed Al, Cu and Ti coatings, Acta Mater. 61 (2013) 6329–6337, https://doi.org/10.1016/j.actamat.2013.06.033.
[5] A.S. Agazhanov, D.A. Samoshkin, Y.M. Kozlovskii, Thermophysical properties of Inconel 718 alloy, J. Phys. Conf. Ser. 1382 (2019) 012175, https://doi.org/10.1088/1742-6596/1382/1/012175.

[6] K. Tan, S. Markovych, W. Hu, O. Shorinov, Y. Wang, Review of manufacturing and repair of aircraft and engine parts based on cold spraying technology and additive manufacturing technology, Aerosp. Tech. Technol. (2020) 53–70, https://doi.org/10.32620/aktt.2020.3.06.

[7] H. Assadi, F. Gärtner, T. Stoltenhoff, H. Kreye, Bonding mechanism in cold gas spraying, Acta Mater. 51 (2003) 4379–4394, https://doi.org/10.1016/S1359-6454(03)00274-X.

[8] T. Schmidt, H. Assadi, F. Gärtner, H. Richter, T. Stoltenhoff, H. Kreye, T. Klassen, From particle acceleration to impact and bonding in cold spraying, J. Therm. Spray Technol. 18 (2009) 794, https://doi.org/10.1007/s11666-009-9357-7.

[9] T. Schmidt, F. Gärtner, H. Assadi, H. Kreye, Development of a generalized parameter window for cold spray deposition, Acta Mater. 54 (2006) 729–742, https://doi.org/10.1016/j.actamat.2005.10.005.

[10] H. Assadi, H. Kreye, F. Gärtner, T. Klassen, Cold spraying – a materials perspective, Acta Mater. 116 (2016) 382–407, https://doi.org/10.1016/j.actamat.2016.06.034.

[11] J. Fiebig, J.-P. Gagnon, G. Mauer, E. Bakan, R. Vaßen, In-flight measurements of particle temperature and velocity with a high-speed IR camera during cold gas spraying of In718 and TiAlCrNb, J. Therm. Spray Technol. 31 (2022) 2013–2024, https://doi.org/10.1007/s11666-022-01426-9.

[12] G. Mauer, R. Singh, K.-H. Rauwald, S. Schrüfer, S. Wilson, R. Vaßen, Diagnostics of cold-sprayed particle velocities approaching critical deposition conditions, J. Therm. Spray Technol. 26 (2017) 1423–1433, https://doi.org/10.1007/s11666-017-0596-8.

[13] H. Fukanuma, N. Ohno, B. Sun, R. Huang, In-flight particle velocity measurements with DPV-2000 in cold spray, Surf. Coat. Technol. 201 (2006) 1935–1941, https://doi.org/10.1016/j.surfcoat.2006.04.035.

[14] M. Faizan-Ur-Rab, S.H. Zahiri, P.C. King, C. Busch, S.H. Masood, M. Jahedi, R. Nagarajah, S. Gulizia, Utilization of titanium particle impact location to validate a 3D multicomponent model for cold spray additive manufacturing, J. Therm. Spray Technol. 26 (2017) 1874–1887, https://doi.org/10.1007/s11666-017-0628-4.

[15] A. Sova, A. Okunkova, S. Grigoriev, I. Smurov, Velocity of the particles accelerated by a cold spray micronozzle: experimental measurements and numerical simulation, J. Therm. Spray Technol. 22 (2013) 75–80, https://doi.org/10.1007/s11666-012-9846-y.

[16] H. Koivuluoto, J. Larjo, D. Marini, G. Pulci, F. Marra, Cold-sprayed Al6061 coatings: online spray monitoring and influence of process parameters on coating properties, Coatings 10 (2020) 348, https://doi.org/10.3390/coatings10040348.

[17] B. Jodoin, F. Raletz, M. Vardelle, Cold spray modeling and validation using an optical diagnostic method, Surf. Coat. Technol. 200 (2006) 4424–4432, https://doi.org/10.1016/j.surfcoat.2005.02.209.

[18] H. Koivuluoto, V. Matikainen, J. Larjo, P. Vuoristo, Novel online diagnostic analysis for in-flight particle properties in cold spraying, J. Therm. Spray Technol. 27 (2018) 423–432, https://doi.org/10.1007/s11666-018-0685-3.

[19] H. Assadi, T. Schmidt, H. Richter, J.-O. Kliemann, K. Binder, F. Gärtner, T. Klassen, H. Kreye, On parameter selection in cold spraying, J. Therm. Spray Technol. 20 (2011) 1161–1176, https://doi.org/10.1007/s11666-011-9662-9.

[20] R. Bolot, S. Deng, Z. Cai, H. Liao, G. Montavon, A coupled model between robot trajectories and thermal history of the workpiece during thermal spray operation, J. Therm. Spray Technol. 23 (2014) 296–303, https://doi.org/10.1007/s11666-013-0048-z.

[21] C.A. Santini, Particle Injection Simulation on Cold Spray Technology, (n.d.) 87.

[22] K. Wittig, A. Golia, P.A. Nikrityuk, 3D numerical study on the influence of particle porosity on heat and fluid flow, Prog. Comput. Fluid Dyn. Int. J. 12 (2012) 207, https://doi.org/10.1504/PCFD.2012.047463.

[23] T. Stoltenhoff, H. Kreye, H.J. Richter, An analysis of the cold spray process and its coatings, J. Therm. Spray Technol. 11 (2002) 542–550, https://doi.org/10.1361/105996302770348682.

[24] S. Yin, M. Meyer, W. Li, H. Liao, R. Lupoi, Gas flow, particle acceleration, and heat transfer in cold spray: a review, J. Therm. Spray Technol. 25 (2016) 874–896, https://doi.org/10.1007/s11666-016-0406-8.

[25] R. Singh, K.-H. Rauwald, E. Wessel, G. Mauer, S. Schruefer, A. Barth, S. Wilson, R. Vassen, Effects of substrate roughness and spray-angle on deposition behavior of cold-sprayed Inconel 718, Surf. Coat. Technol. 319 (2017) 249–259, https://doi.org/10.1016/j.surfcoat.2017.03.072.

[26] S.V. Klinkov, V.F. Kosarev, N.S. Ryashin, V.S. Shikalov, Influence of particle impact angle on formation of profile of single coating track during cold spraying, in: Novosibirsk, Russia, 2018, p. 020007, https://doi.org/10.1063/1.5065085.

[27] C.-J. Li, W.-Y. Li, Y.-Y. Wang, G.-J. Yang, H. Fukanuma, A theoretical model for prediction of deposition efficiency in cold spraying, Thin Solid Films 489 (2005) 79–85, https://doi.org/10.1016/j.tsf.2005.05.002.

[28] S. James, K. Shah, Effect of velocity and impact angle on residual stress generation in cold spray process – a molecular dynamics simulation study, Proc. Manuf. 48 (2020) 776–780, https://doi.org/10.1016/j.promfg.2020.05.113.

[29] D. Edgington-Mitchell, D.R. Honnery, J. Soria, The underexpanded jet Mach disk and its associated shear layer, Phys. Fluids 26 (2014) 096101, https://doi.org/10.1063/1.4894741.

[30] B. Pavel Viktorovich, U.V. Nikolaevich, Mach reflection of a shock wave from the symmetry axis of the supersonic nonisobaric jet, Res. J. Appl. Sci. Eng. Technol. 8 (2014) 135–142, https://doi.org/10.19026/rjaset.8.951.

[31] J.-J. Park, M.-W. Lee, S.S. Yoon, H.-Y. Kim, S.C. James, S.D. Heister, S. Chandra, W.-H. Yoon, D.-S. Park, J. Ryu, Supersonic nozzle flow simulations for particle coating applications: effects of shockwaves, nozzle geometry, ambient pressure, and substrate location upon flow characteristics, J. Therm. Spray Technol. 20 (2011) 514–522, https://doi.org/10.1007/s11666-010-9542-8.

[32] J. Pattison, S. Celotto, A. Khan, W. O'Neill, Standoff distance and bow shock phenomena in the cold spray process, Surf. Coat. Technol. 202 (2008) 1443–1454, https://doi.org/10.1016/j.surfcoat.2007.06.065.

[33] A. Nastic, B. Jodoin, Evaluation of heat transfer transport coefficient for cold spray through computational fluid dynamics and particle in-flight temperature measurement using a high-speed IR camera, J. Therm. Spray Technol. 27 (2018) 1491–1517, https://doi.org/10.1007/s11666-018-0787-y.

[34] H. Takana, H. Li, K. Ogawa, T. Kuriyagawa, H. Nishiyama, Computational and experimental studies on cavity filling process by cold gas dynamic spray, J. Fluids Eng. 132 (2010) 021302, https://doi.org/10.1115/1.4000802.

[35] Y. Changfu, Q. Haiying, X. Xuchang, Lift force on rotating sphere at low Reynolds numbers and high rotational speeds, Acta Mech. Sinica 19 (2003) 300–307, https://doi.org/10.1007/BF02487805.

[36] S. Zhou, G. Zhang, X. Xu, Experiments on the drag and lift coefficients of a spinning sphere, Water 14 (2022) 2593, https://doi.org/10.3390/w14172593.

[37] P.K. Gupta, K.V. Pagalthivarthi, Effect of Model Lift Coefficients on Particle Trajectory, 2005.

[38] C. Cao, W. Li, Z. Zhang, X. Yang, Y. Xu, Cold spray additive manufacturing of Ti6Al4V: special nozzle design using numerical simulation and experimental validation, Coatings 12 (2022) 210, https://doi.org/10.3390/coatings12020210.

[39] S. Garmeh, M. Jadidi, A. Dolatabadi, Three-dimensional modeling of cold spray for additive manufacturing, J. Therm. Spray Technol. 29 (2020) 38–50, https://doi.org/10.1007/s11666-019-00928-3.

[40] R.N. Raoelison, Ch. Verdy, H. Liao, Cold gas dynamic spray additive manufacturing today: deposit possibilities, technological solutions and viable applications, Mater. Des. 133 (2017) 266–287, https://doi.org/10.1016/j.matdes.2017.07.067.

[41] J. Schmitt, J. Fiebig, S. Schrüfer, O. Guillon, R. Vaßen, Adjusting residual stresses during cold spray deposition of IN718, J. Therm. Spray Technol. (2023), https://doi.org/10.1007/s11666-023-01673-4.

[42] S. Lett, A. Quet, S. Hémery, J. Cormier, E. Meillot, P. Villechaise, Residual stresses development during cold spraying of Ti-6Al-4V combined with in situ shot peening, J. Therm. Spray Technol. (2022), https://doi.org/10.1007/s11666-022-01514-w.

[43] A. Fardan, C.C. Berndt, R. Ahmed, Numerical modelling of particle impact and residual stresses in cold sprayed coatings: a review, Surf. Coat. Technol. 409 (2021) 126835, https://doi.org/10.1016/j.surfcoat.2021.126835.

[44] W. Ma, Y. Xie, C. Chen, H. Fukanuma, J. Wang, Z. Ren, R. Huang, Microstructural and mechanical properties of high-performance Inconel 718 alloy by cold spraying, J. Alloys Compd. 792 (2019) 456–467, https://doi.org/10.1016/j.jallcom.2019.04.045.

[45] O.C. Ozdemir, C.A. Widener, Influence of powder injection parameters in high-pressure cold spray, J. Therm. Spray Technol. 26 (2017) 1411–1422, https://doi.org/10.1007/s11666-017-0606-x.

[46] A. Sova, I. Smurov, M. Doubenskaia, P. Petrovskiy, Deposition of aluminum powder by cold spray micronozzle, Int. J. Adv. Manuf. Technol. 95 (2018) 3745–3752, https://doi.org/10.1007/s00170-017-1443-2.

[47] A. Sova, S. Klinkov, V. Kosarev, N. Ryashin, I. Smurov, Preliminary study on deposition of aluminium and copper powders by cold spray micronozzle using helium, Surf. Coat. Technol. 220 (2013) 98–101, https://doi.org/10.1016/j.surfcoat.2012.09.036.

[48] A. Nastic, B. Jodoin, D. Poirier, J.-G. Legoux, Particle temperature effect in cold spray: a study of soft particle deposition on hard substrate, Surf. Coat. Technol. 406 (2021) 126735, https://doi.org/10.1016/j.surfcoat.2020.126735.

[49] R. Vaßen, J. Fiebig, T. Kalfhaus, J. Gibmeier, A. Kostka, S. Schrüfer, Correlation of microstructure and properties of cold gas sprayed INCONEL 718 coatings, J. Therm. Spray Technol. 29 (2020) 1455–1465, https://doi.org/10.1007/s11666-020-00988-w.

[50] Tagungsunterlagen, 12. Kolloquium Hochgeschwindigkeits-Flammspritzen: 26. und 27, in: Oktober 2023, Erding = Conference Proceedings: HVOF Spraying, Gemeinschaft Thermisches Spritzen e.V, Unterschleißheim, Germany, 2023.

[51] G.G. Stoney, The tension of metallic films deposited by electrolysis, Proc. R. Soc. Lond. Ser. Contain. Pap. Math. Phys. Character 82 (1909) 172–175.

[52] M. Mutter, G. Mauer, R. Mücke, R. Vaßen, H.C. Back, J. Gibmeier, Investigations on the initial stress Evolution during atmospheric plasma spraying of YSZ by in situ curvature measurement, J. Therm. Spray Technol. 25 (2016) 672–683, https://doi.org/10.1007/s11666-016-0398-4.

[53] L. Davidson, Fluid Mechanics, Turbulent Flow and Turbulence Modeling, 2020.

[54] F.R. Menter, Two-equation eddy-viscosity turbulence models for engineering applications, AIAA J. 32 (1994) 1598–1605, https://doi.org/10.2514/3.12149.

[55] D. Adanta, I.M.R. Fattah, N.M. Muhammad, Comparison of Standard k-ε and SST k-ω Turbulence Model for Breastshot Waterwheel Simulation, 2020.

[56] Menter, F.R., Kuntz, M., Langtry, R. Ten years of industrial experience with the SST turbulence model. Heat Mass Transf. (n.d.).

[57] G. Perez, A Brief Overview of the Drag Laws Used in the Lagrangian Tracking of Ash Trajectories for Boiler Fouling CFD Models, 2016, p. 15.

[58] S.A. Morsi, A.J. Alexander, An investigation of particle trajectories in two-phase flow systems, J. Fluid Mech. 55 (1972) 193–208, https://doi.org/10.1017/S0022112072001806.

[59] S.I. Rubinow, J.B. Keller, The transverse force on a spinning sphere moving in a viscous fluid, J. Fluid Mech. 11 (1961) 447, https://doi.org/10.1017/S0022112061000640.

[60] W.-Y. Li, C.-J. Li, Optimal design of a novel cold spray gun nozzle at a limited space, J. Therm. Spray Technol. 14 (2005) 391–396, https://doi.org/10.1361/105996305X59404.

[61] M.W. Lee, J.J. Park, D.Y. Kim, S.S. Yoon, H.Y. Kim, D.H. Kim, S.C. James, S. Chandra, T. Coyle, J.H. Ryu, W.H. Yoon, D.S. Park, Optimization of supersonic

nozzle flow for titanium dioxide thin-film coating by aerosol deposition, J. Aerosol Sci. 42 (2011) 771–780, https://doi.org/10.1016/j.jaerosci.2011.07.006.
[62] T. Han, Z. Zhao, B.A. Gillispie, J.R. Smith, Effects of spray conditions on coating formation by the kinetic spray process, J. Therm. Spray Technol. 14 (2005) 373–383, https://doi.org/10.1361/105996305X59369.
[63] F. Lang, J.-C. Schmitt, S. Cabeza, T. Pirling, J. Fiebig, R. Vassen, J. Gibmeier, IN718 cold gas repair spray of large cavities—microstructure and residual stresses, in: E. A. Ott, J. Andersson, C. Sudbrack, Z. Bi, K. Bockenstedt, I. Dempster, M. Fahrmann, P. Jablonski, M. Kirka, X. Liu, D. Nagahama, T. Smith, M. Stockinger, A. Wessman (Eds.), Proc. 10th Int. Symp. Superalloy 718 Deriv., Springer Nature Switzerland, Cham, 2023, pp. 739–753, https://doi.org/10.1007/978-3-031-27447-3_44.